Fabrication and luminescent properties of erbium doped Y_2O_3-MgO and Gd_2O_3-MgO nanocomposite ceramics

Stanislav Balabanov[a], Dmitry Permin[a,b,*], Simone Normani[c], Alexander Belyaev[a], Vitaliy Koshkin[a,b], Pavel Andreev[b], Igor Ladenkov[f], Alain Braud[c], Patrice Camy[c], Rosa Maria Solé[d], Xavier Mateos[d], and Pavel Loiko[c]

[a]*G.G. Devyatykh Institute of Chemistry of High-Purity Substances of the RAS, 49 Tropinin St., 603137 Nizhny Novgorod, Russia*
[b]*N.I. Lobachevsky National Research University, 23a Gagarin Ave., 603022 Nizhny Novgorod, Russia*
[c]*Centre de Recherche sur Les Ions, Les Matériaux et La Photonique (CIMAP), UMR 6252 CEA-CNRS-ENSICAEN, Université de Caen, 6 Boulevard Maréchal Juin, 14050 Caen, France*
[d]*Universitat Rovira I Virgili (URV), Física I Cristal·lografia de Materials I Nanomaterials (FiCMA-FiCNA)-EMaS, Marcel·lí Domingo 1, 43007 Tarragona, Spain*
[e]*Joint-stock company Research and Production Enterprise "Salut", 7 Larin St., 603950 Nizhny Novgorod, Russia*
**Corresponding author, e-mail: permin@ihps-nnov.ru*

Abstract: We report on the fabrication and optical properties of erbium-doped Y_2O_3-MgO and Gd_2O_3-MgO nanocomposite ceramics, with a particular focus on their mid-infrared emission. The ceramics were fabricated by a self-propagating high temperature synthesis followed by hot pressing. The transmittance of 1.7 mm-thick 5 at.% Er:Y_2O_3-MgO and 7 at.% Er:Gd_2O_3-MgO ceramics at 3 µm amounted to 79.4% and 21.5%, respectively. This difference in transmission, as revealed by microstructural analysis, is due to variation in the distribution of residual pore sizes, while the average grain size is almost the same for both ceramics, being ~200 nm. The composites exhibited luminescence in the visible, near-infrared, and mid-infrared spectral ranges attributed to electronic transitions of Er^{3+} ions in the cubic sesquioxide phase. However, some peculiarities in the Raman and luminescence spectra were identified as compared to single-phase Er:Y_2O_3 and Er:Gd_2O_3 ceramics. Together with XRD studies and SEM/EDX elemental distribution maps, this may indicate certain solubility of MgO in the sesquioxide phase of the composites.

Keywords: composites; optical ceramics; sesquioxides; erbium ions; luminescence; mid-infrared.

1. Introduction

The development of ceramic technology has led to significant advances in the production of solid-state laser materials [1,2]. Until recently, the range of potential polycrystalline optical media was limited to single-phase materials with a cubic crystal lattice, since the anisotropy of other types of structures leads to passive optical losses due to light scattering and / or birefringence. Several approaches have been developed to fabricate non-cubic optical (including laser) ceramics by orienting the grains [3] or limiting their size during sintering [4]. This reduces passive optical losses in ceramics, especially in the near and mid-infrared spectral ranges. For example, the ceramics alumina (Al_2O_3) [4], tetragonal yttria-stabilized zirconia (Y-TZP) [5], Yb^{3+}-doped fluorapatite (FAP) [6], Nd^{3+}- [7] or Er^{3+}-doped [8] strontium fluorapatite (S-FAP), strontium fluoroarsenate (SFAs) [9] have been fabricated in this way, and laser emission has been achieved on fluorapatite samples doped with ytterbium [6] and neodymium [10] ions.

Another way to expand the range of optical materials is to create ceramics with a composite structure so that by limiting the grain size to the nm level, it is possible to create highly transparent materials in the infrared. The most successful examples of such ceramics are the nanocomposites of cubic rare earth sesquioxides and magnesium oxide, such as Y_2O_3-MgO (yttria - magnesia) [11], Gd_2O_3-MgO (gadolinia - magnesia) [12], Dy_2O_3-MgO (dysprosia - magnesia) [13], Sc_2O_3-MgO (scandia - magnesia), and Lu_2O_3-MgO (lutetia - magnesia) [14]. The luminescent properties of such composite materials doped with optically active rare earth ions (RE^{3+}) have recently gained significant attention. In particular, Safronova *et al*. [15] and later Wang *et al.* [16] demonstrated intense luminescence at ~1.93 and 2.12 μm from Ho:Y_2O_3-MgO ceramics. Blair *et al.* [17] and Ma *et al.* [18] performed optical spectroscopy measurements of the $^4I_{13/2} \rightarrow {}^4I_{15/2}$ transition (at ~1.55 μm) of Er^{3+} ions in Y_2O_3-MgO ceramics. Due to the fact that RE^{3+} ions are practically insoluble in MgO, the absorption and luminescence spectra of RE:Y_2O_3-MgO nanocomposites greatly resemble those of RE:Y_2O_3 ceramics.

In addition to the $^4I_{13/2} \rightarrow {}^4I_{15/2}$ transition at ~1.55 μm, Er^{3+} ions exhibit another laser transition of interest, namely $^4I_{11/2} \rightarrow {}^4I_{13/2}$, falling into the mid-infrared spectral range at ~2.80 μm [19]. The number of efficient laser materials in this range is rather limited, so the search for new ones is of great importance. Er^{3+}-doped nanocomposites Y_2O_3-MgO and Gd_2O_3-MgO can be of particular interest for mid-infrared emission, since the light scattering in these materials decreases significantly with increasing the wavelength. Both yttria and gadolinia are attractive matrices for doping with Er^{3+} ions for several reasons, namely (i) they possess one of the lowest phonon energies among oxide materials, which reduces the rates of multiphonon non-radiative relaxation from the $^4I_{11/2}$ excited-state; (ii) they allow for high Er^{3+} doping levels, which is particularly important for increasing the efficiency of energy-transfer upconversion from the metastable intermediate $^4I_{13/2}$ state, avoiding the bottleneck effect for the self-terminating $^4I_{11/2} \rightarrow {}^4I_{13/2}$ transition; (iii) they have good thermal and mechanical properties and they are chemical inert.

The higher thermal conductivity of nanocomposites as compared to single-phase sesquioxide ceramics is considered as the main advantage of such materials and is relevant for potential laser applications. Indeed, at room temperature, the thermal conductivity of Er:Y_2O_3-MgO ceramics is two times higher than that of Er:Y_2O_3 [18]. However, the situation is likely to be reversed when the active element is cooled [20,21].

The fabrication of bulk optical material Er:Gd_2O_3, both in the form of single-crystals and ceramics, is hindered by the low phase-transition temperature of ~1200 °C. In the case

of the Gd_2O_3-MgO composite, however, the phase transition in Gd_2O_3 occurs without breaking the integrity of the sample. The annealing conditions can control the ratio of monoclinic and cubic phases in the composite. This is another way to expand the range of optical materials doped with Er^{3+} ions.

The aim of the present work was to fabricate Er:Y_2O_3-MgO and Er:Gd_2O_3-MgO composite ceramics and to study their optical properties, in particular focusing on their mid-infrared emission properties around ~2.8 μm.

2. Synthesis of ceramics

The starting materials used in this work were yttria Y_2O_3 (99.99% Polirit, Russia), gadolinia Gd_2O_3 (99.99% Polirit, Russia), erbia Er_2O_3 (99.99% Polirit, Russia), magnesia MgO (99.99% Unikhim, Russia), nitric acid HNO_3 (99.9999% Khimreaktiv, Russia), and aminoacetic acid NH_2CH_2COOH (99.9% Khimreaktiv, Russia).

Er:Y_2O_3-MgO and Er:Gd_2O_3-MgO starting powders were prepared by a self-propagating high-temperature synthesis (SHS) process described in detail previously [22,23]. In short, yttrium, gadolinium, erbium, and magnesium nitrates were prepared each by dissolving the corresponding oxide in nitric acid. The optimum volume ratio of yttria (gadolinia) to magnesia in infrared-transparent ceramics is 50:50 [11,24]. Er:Y_2O_3-MgO and Er:Gd_2O_3-MgO ceramics were obtained with the same ratio, assuming that erbia (Er_2O_3) dissolves only in yttria or gadolinia. The densities of Er:Y_2O_3 and Er:Gd_2O_3 solid solutions were calculated by the additive method. The nitrates of rare earths (RE) and magnesium were mixed in a given ratio, and then aminoacetic acid was added to the resulting solution according to the stoichiometry of the following reactions:

$6RE(NO_3)_3 + 10NH_2CH_2COOH \rightarrow 3RE_2O_3 + 20CO_2 + 25H_2O + 14N_2$,

$9Mg(NO_3)_2 + 10NH_2CH_2COOH \rightarrow 9MgO + 20CO_2 + 25H_2O + 14N_2$.

The solutions were evaporated at 110 °C. Next, to initiate SHS, the quartz flask containing the precursors was placed in a furnace preheated to 500 °C. The combustion process resulted in the formation of a soft foam consisting of RE_2O_3-MgO nanopowders. After synthesis, the powders were annealed in air in a muffle furnace at a temperature of 800 °C for 5 hours (h).

The annealed powders were compacted in a 15 mm diameter stainless steel mold at 40 MPa. The green bodies obtained in this way were consolidated by hot pressing (HP) under ≤10 Pa vacuum in a graphite mold at temperatures of 1450°C (for Er:Y_2O_3-MgO) and 1400 °C (for Er:Gd_2O_3-MgO) and a uniaxial pressure of 50 MPa, using home-made equipment. The green bodies were isolated with graphite paper to reduce the interaction between the mold material and the ceramic samples. The heating schedule included an isothermal hold at 800 °C for 20 min to desorb moisture and carbon dioxide, heating to sintering temperature at a rate of 20 °C/min, holding for 60 min, and free cooling. The initial uniaxial pressure applied to the green bodies was 3 MPa. After the temperature reached 900 °C, the uniaxial pressure was increased to its maximum at a rate of 1 MPa/min. The samples were further annealed in air at 1100 °C for 5 h in a muffle furnace to remove oxygen vacancies and carbon impurities. The thickness of the polished ceramic samples was 1.7 mm. Ceramics with the compositions of 1 at.%, 3 at.%, 5 at.%, and 7 at.% Er:Y_2O_3-MgO and 7 at.% Er:Gd_2O_3-MgO were fabricated. Here, the percentages represent the number of yttrium/gadolinium atoms replaced by erbium.

3. Experimental

The X-ray diffraction (XRD) measurements for the powders and ceramics were performed using an XRD-7000 diffractometer (Shimadzu, Kyotocity, Japan), CuKα radiation, 30 kV/40 mA. The scans were performed in the Bragg-Brentano geometry in the range of diffraction angles 2θ of 20°–80° with the step of 0.04° and an exposure time of 1-3 s. The qualitative phase analysis was carried out using the PDF-2 database (ICDD, 2012). The cell parameters refinement was carried out by the Rietveld method using the Diffrac.TOPAS software (Bruker, Karlsruhecity, Germany) with the following cif-files from the ICSD database (2016): MgO (# 64930), Y_2O_3 (# 82420), cubic-Gd_2O_3 (# 41270), and monoclinic-Gd_2O_3 (# 636103).

The specific surface areas (S_{BET}) of the SHS powders were measured by nitrogen adsorption according to the Brunauer-Emmett-Teller (BET) method using Meta Sorbi-MS equipment. The average BET-equivalent particle diameter (d_{BET}, in nm) was calculated assuming their spherical shape according to the following equation: $d_{BET} = 6000/(\rho \times S_{BET})$, where ρ is the theoretical density of the material calculated by the additive method. The densities of the sintered samples were determined by hydrostatic weighing in distilled water on a Sartorius CPA balance (Sartorius, Germany) with an accuracy of 0.005 g/cm^3, which is ~0.1% of the theoretical density of the composites. The microstructure of the composites was examined on an Auriga CrossBeam scanning electron microscope (SEM) (Carl Zeiss, Germany) operated at an accelerating voltage of 3 keV using a secondary electron detector. The average grain size was determined by measuring the width of a minimum of 200 grains. No shape factor was applied. The Energy Dispersive X-ray (EDX) based element mapping was studied with a FEI Scios 2 Field Emission Scanning Electron Microscope with a focused Gallium ion beam (FESEM-FIB).

The infrared spectra of the RE_2O_3-MgO composite ceramics were recorded on an FT-801 Fourier transform IR spectrometer (Simex, Russia). The Raman spectra were measured using a confocal Raman microscope (inVia, Renishaw) equipped with a ×50 objective (Leica) and an Ar^+ ion laser (457.0 nm).

The spectra of optical absorption in the near-IR were measured using a Perkin-Elmer LAMBDA 1050 spectrophotometer with a resolution of 1 nm.

The luminescence spectra in the mid-infrared were measured using a home-made set-up. It included a Ti:Sapphire laser (Mira, Coherent) tuned to ~0.96 μm, a large mode area ZrF_4 fiber for light collection and an optical spectrum analyzer (OSA, Yokogawa AQ6376) purged with N_2 gas to eliminate the structured water vapor absorption in the air. The effect of the residual water absorption was further removed by calibrating the OSA spectral response with a 20 W quartz lamp.

The luminescence decay was studied under excitation by a ns optical parametric oscillator (Horizon, Continuum), and the decay curves were measured employing a 1/4 m monochromator (Oriel 77200), an InGaAs detector with a preamplifier and an 8 GHz oscilloscope (DSA70804B, Tektronix).

4. Results and discussion

4.1. Er:Y_2O_3-MgO and Er:Gd_2O_3-MgO powders

The SHS powders were calcined in air at 800 °C for 5 h immediately prior to hot pressing. This mode was previously developed for undoped Y_2O_3-MgO powders [22] and allows the removal of residual carbon-containing substances as much as possible while maintaining nm-sized particles within the powders and, consequently, preserving their high sinterability. The specific surface areas S_{BET} of the powders after calcination were 27 and 25

m^2/g for Er:Y_2O_3-MgO and Er:Gd_2O_3-MgO, respectively. This is not much different from the values for undoped powders, amounting to 34 and 23 m^2/g, respectively, and is probably due to variations in the SHS synthesis conditions rather than the effect of erbium oxide. The corresponding average BET-equivalent particle diameters d_{BET} were 50 nm for Er:Y_2O_3-MgO and 42 nm for Er:Gd_2O_3-MgO powders.

The XRD patterns for Er:Y_2O_3-MgO, Er:Gd_2O_3-MgO and undoped powders are shown in Fig. 1, and the unit-cell parameters are summarized in Table 1. Only cubic phases are observed in the XRD patterns: cubic RE_2O_3 with a space group $Ia\bar{3}$ adopting the body-centered bixbyite (C-type) structure and cubic MgO with a space group *Fm-3m* with a NaCl-type structure. The proximity between the ionic radii of Er^{3+} (0.89 Å) dopant ions and those of Y^{3+} (0.90 Å) and Gd^{3+} (0.938 Å) host-forming cations (all values correspond to VI-fold coordination by oxygen), causes very small changes in the unit-cell parameters as a result of Er^{3+} doping. Although the cell size of doped sesquioxides slightly decreased as expected, these changes are within the measurement error interval. Due to the nanoscale nature of the powders, the diffraction peaks are low in intensity and significantly broadened.

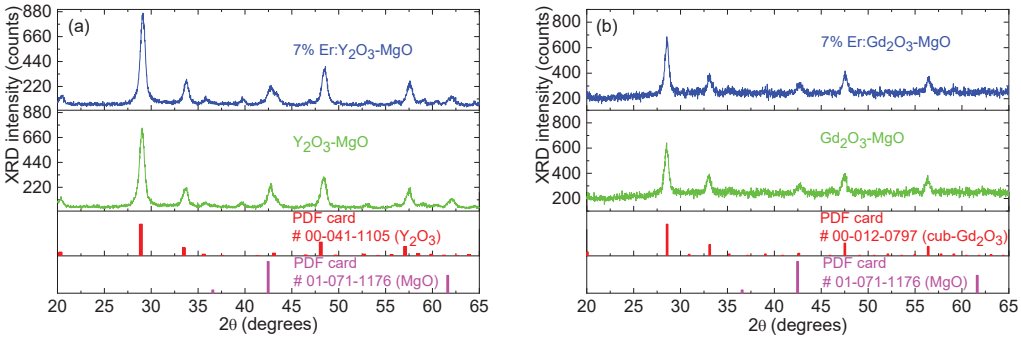

Figure 1. XRD patterns of Er:Y_2O_3-MgO and Er:Gd_2O_3-MgO nanopowders obtained by self-propagating high-temperature synthesis. *Vertical dashes* - standard reflections for Y_2O_3 (PDF # 00-041-1105), Gd_2O_3 (PDF # 00-012-0797) and MgO (PDF # 01-071-1176).

Table 1. XRD analysis of Er:Y_2O_3-MgO and Er:Gd_2O_3-MgO nanopowders.

Powder	Unit-cell parameter *a*, Å		
	Y_2O_3	MgO	Gd_2O_3
Y_2O_3-MgO	10.612(21)	4.221(9)	-
Er:Y_2O_3-MgO	10.597(3)	4.215(1)	-
Gd_2O_3-MgO	-	4.217(16)	10.81(4)
Er:Gd_2O_3-MgO	-	4.219(5)	10.797(12)

4.2. Microstructure of Er:Y_2O_3-MgO and Er:Gd_2O_3-MgO ceramics

The XRD powder analysis of the Er:Y_2O_3-MgO and Er:Gd_2O_3-MgO ceramics is shown in Fig. 2. There are no changes in the phase composition of the Er:Y_2O_3-MgO ceramics compared to the starting powders. It remains biphasic, based on cubic Y_2O_3 and cubic MgO. According to Vegard's rule, the unit-cell parameter for a solid-solution of 7 mol.% Er_2O_3 in Y_2O_3 should be a = 10.606 Å, while our measured value is a = 10.579(2) Å; for magnesia, the standard value is a = 4.217 Å, and that measured for ceramics is a = 4.215(2) Å. A noticeable distortion of the Er:Y_2O_3 unit cell can be caused by partial dissolution of magnesia in yttria, which is also supported by the SEM/EDX element distribution maps discussed below.

The ceramic Er:Gd_2O_3-MgO is also biphasic, but if MgO remains cubic, then Er:Gd_2O_3 is completely (within the error of the XRD analysis) in the monoclinic phase with a space group

of *C*2/*m* with Sm_2O_3-type (B-type) structure. Table 2 lists the unit-cell parameters of this phase in comparison with the standard ones for monoclinic erbia and gadolinia. A stronger decrease of the cell volume than that expected for 7 mol.% Er_2O_3 in Gd_2O_3 solid solution can be explained, as in the case of Er:Y_2O_3-MgO, by the partial dissolution of magnesia in gadolinia. The unit-cell parameter of magnesia is a = 4.213(2) Å, which is only slightly different from the standard one.

Table 2. Unit-cell parameters of the monoclinic Er:Gd_2O_3 phase constituting the composite 7 at.% Er:Gd_2O_3-MgO.

Er_2O_3-Gd_2O_3 solid solution (B-type) within the composite 7 at.% Er:Gd_2O_3-MgO	**Gd_2O_3 (B-type) ICSD 636103**	**Er_2O_3 (B-type) ICSD 419435**
a = 14.059(2) Å	a = 14.091 Å	a = 13.871 Å
b = 3.565(2) Å	b = 3.574 Å	b = 3.468 Å
c = 8.741(2) Å	c = 8.761 Å	c = 8.564 Å
γ = 100(3)°	γ = 100.04°	γ = 100.17°
V = 431.1(1) Å^3	V = 434.4 Å^3	V = 405.5 Å^3

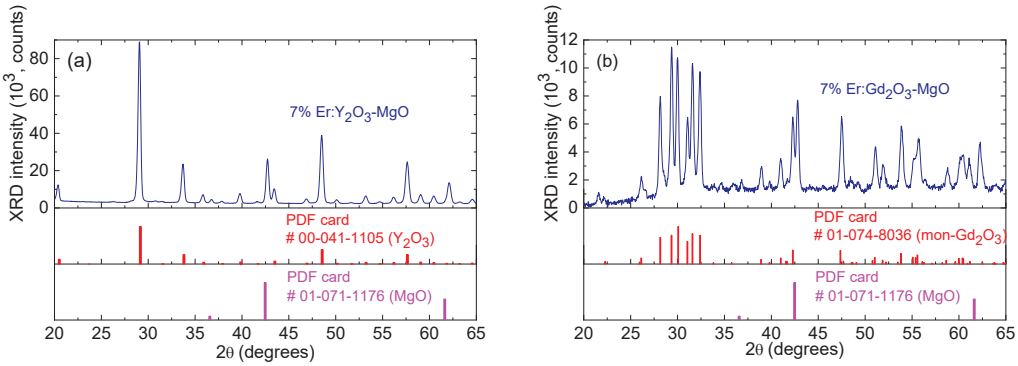

Figure 2. X-ray powder diffraction patterns of (a) Er:Y_2O_3–MgO and (b) Er:Gd_2O_3–MgO ceramics. *Vertical dashes* - standard reflections for cubic Y_2O_3 (PDF # 00-041-1105), monoclinic Gd_2O_3 (PDF # 01-074-8036) and MgO (PDF # 01-071-1176).

Figure 3 shows the SEM/EDX element distribution maps and EDX spectra measured for the Er:Y_2O_3-MgO and Er:Gd_2O_3-MgO ceramics. Although the small size of the grains makes the picture of the element distribution blurred, there are some regularities that agree with the XRD analysis of the ceramics, as well as with literature data. For example, rare-earth atoms are predominantly found in localized regions (separate grains), while magnesium ones are more homogeneously distributed. This may indicate some solubility of magnesium in sesquioxide phases and the fact that the composites consist of phases of (i) MgO and (ii) solid solutions of MgO and Er_2O_3 in Y_2O_3 (or Gd_2O_3). We suggest that the magnesium content in the solid solutions is rather small. It is known that the maximum solubility of ~5 mol.% MgO in Er_2O_3, ~7 mol.% in Y_2O_3 and ~2.5% in Gd_2O_3 is reached at high temperatures around ~2100 °C [25,26] and rapidly decreases with decreasing temperature.

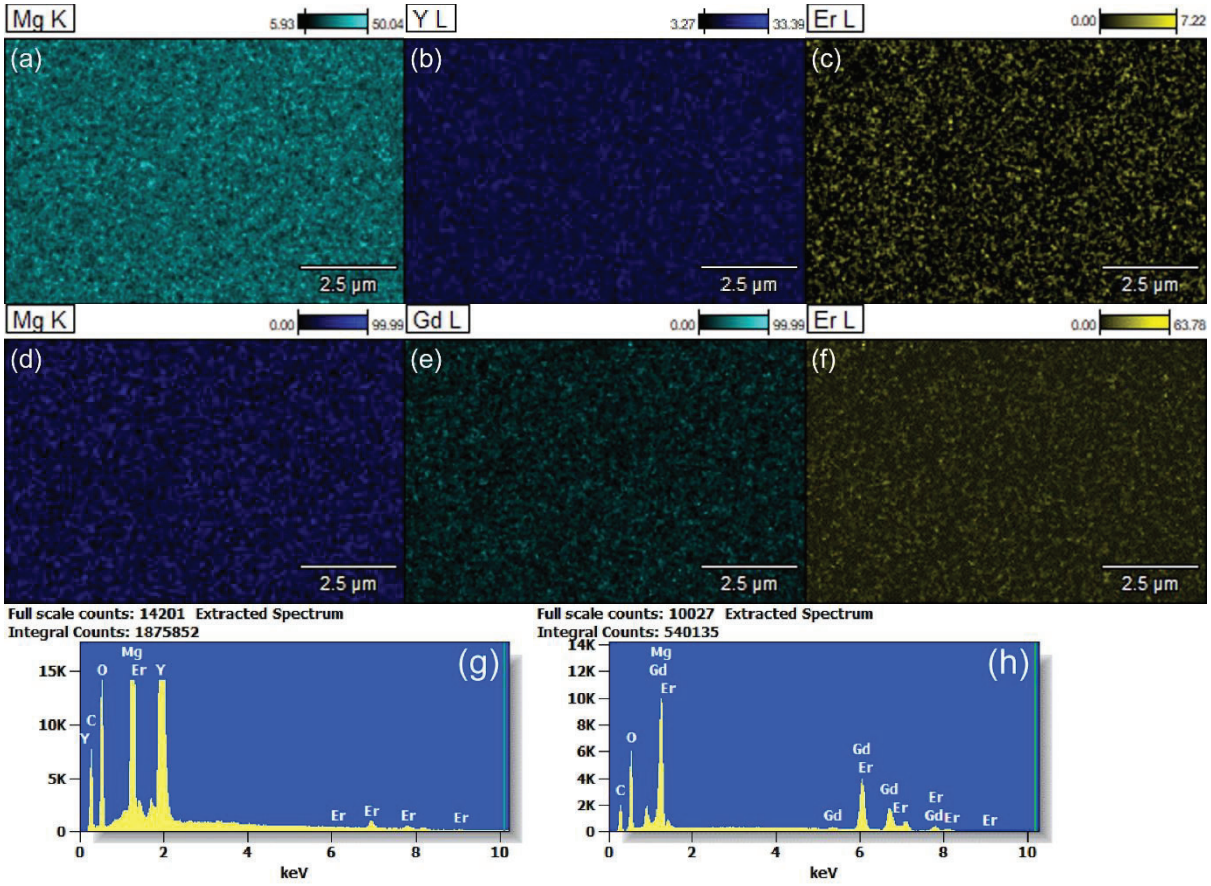

Figure 3. SEM/EDX elemental distribution maps in (a-c) Er:Y_2O_3-MgO and (d-f) Er:Gd_2O_3-MgO ceramics: (a,d) Mg K; (b,e) Gd L and (c,f) Er L. EDX spectra of (g) Er:Y_2O_3-MgO and (h) Er:Gd_2O_3-MgO ceramics.

Figure 4 shows the typical SEM images of the fractured surfaces of the Er:Y_2O_3-MgO and Er:Gd_2O_3-MgO ceramics. It can be seen that the pores in the Er:Y_2O_3-MgO ceramic, Fig. 4(a), are homogeneously distributed and there are almost no pores larger than the grains. In the Er:Gd_2O_3-MgO ceramic, Fig. 4(b), despite similar total porosity, the pores are homogeneously distributed, but there are voids as large as several grains. As will be shown below, this results in increased light scattering, especially at short wavelengths. In the fracture structure of the Er:Y_2O_3-MgO ceramic, as in undoped samples [22], intragranular fracture is observed on the Er:Y_2O_3 grains. However, a rather large number of intragranular fractures on MgO grains is atypical. Usually, the strength of MgO grains is much higher than that of the rare-earth sesquioxides, so they remain intact. The average grain size is ~206 nm, and the grain size distribution is narrow for both phases.

The fracture of the Er:Gd_2O_3-MgO ceramic is also slightly different from that of the undoped samples [23]. As expected, intergranular fractures of magnesia grains are observed, but the destruction of the Er:Gd_2O_3 solid solution occurs through the volume of the grain. This is probably due to stresses in the monoclinic Er:Gd_2O_3 solid solution, as shown by the XRD analysis. Although the hot-pressing temperature was 50 °C lower, the average grain size of ~199 nm is almost the same as that of the yttria-based composite.

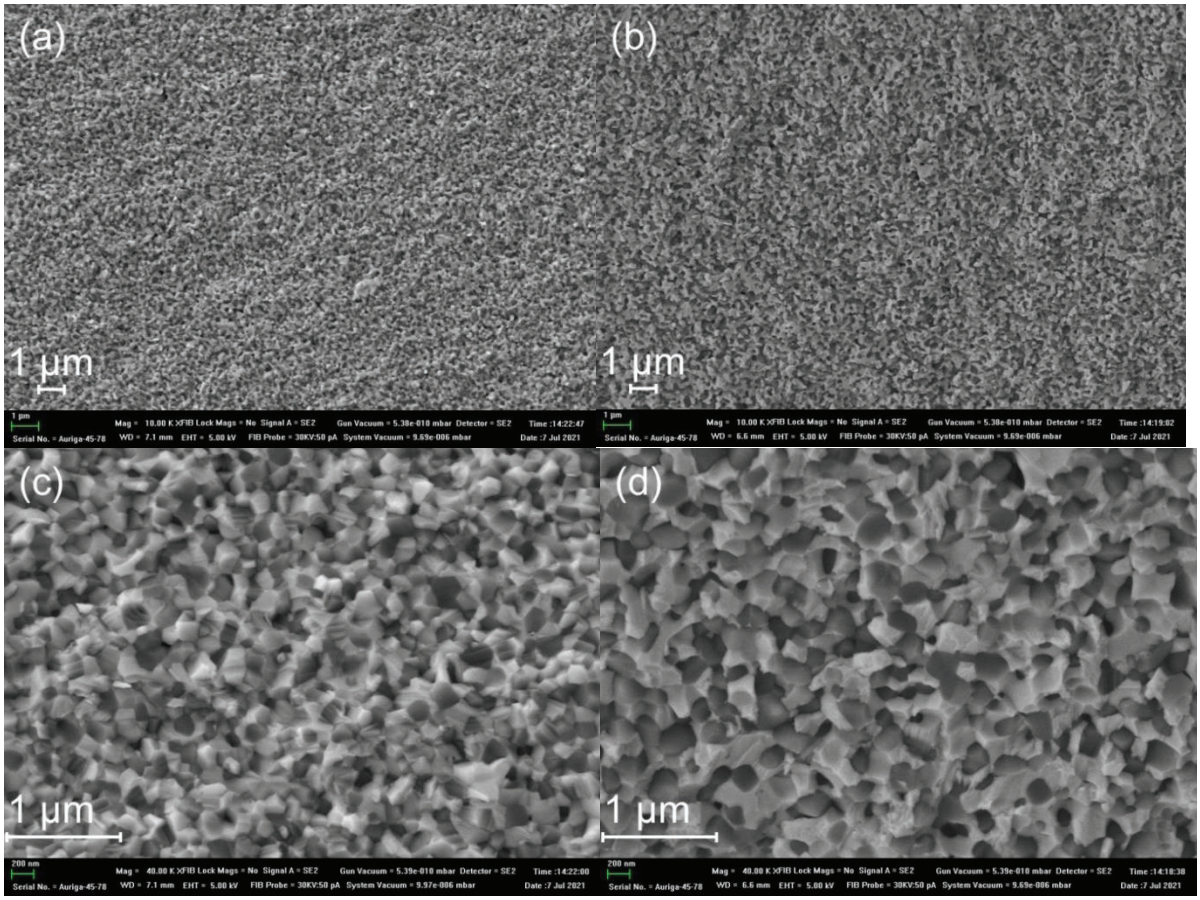

Figure 4. SEM images of the fracture surfaces of hot-pressed (a,c) Er:Y_2O_3-MgO and (b,d) Er:Gd_2O_3-MgO ceramics.

4.3. Spectroscopy of Er:Y_2O_3-MgO and Er:Gd_2O_3-MgO ceramics

Figure 5 shows the IR transmission spectra of Er:Y_2O_3-MgO and Er:Gd_2O_3-MgO ceramics. The addition of erbia did not lead to any peculiarities in the transmission spectrum compared to the undoped composites, except for the absorption band of Er^{3+} ions at ~1.5 µm associated with the $^4I_{15/2} \rightarrow {}^4I_{11/2}$ transition. This band is not visible for the Er:Gd_2O_3-MgO ceramic due to higher light scattering in this spectral range. The absorption lines observed at 4.94 µm are associated with carbon (II) oxide trapped in the pores, and those in the region of 7 µm - with magnesium and/or rare-earth metals carbonates [27]. The noticeably stronger light scattering in the Er:Gd_2O_3-MgO ceramic, as demonstrated above, is due to a wider pore-size distribution compared to the Er:Y_2O_3-MgO composites. The transparency range of both composites extends up to 9 µm. Around 3 µm, the transmittance of the 5 at.% and 7 at.% Er:Y_2O_3-MgO ceramics reaches 79.4% and 78.0%, respectively.

For laser applications of Er:RE_2O_3-MgO composites, it is essential to ensure high transparency at the envisioned laser and pump wavelengths. Mid-infrared Er lasers operating on the $^4I_{11/2} \rightarrow {}^4I_{13/2}$ transition can be pumped at 0.98 µm (to the upper laser level, $^4I_{11/2}$) or at 1.5 µm (to the terminal laser manifold, $^4I_{13/2}$, employing an efficient energy-transfer upconversion process, $^4I_{13/2} + {}^4I_{13/2} \rightarrow {}^4I_{15/2} + {}^4I_{9/2}$). For the developed materials, the former pumping scheme looks more promising as it is expected to correspond to much lower light scattering for the pump radiation. Still, the level of scattering losses around 1.5 µm has to be lowered by optimizing the synthesis conditions.

Previous studies revealed the possibility to attain relatively high transparency (~70%) in the short-wave infrared for undoped 1 mm-thick Y_2O_3-MgO [28] and Gd_2O_3-MgO [29] composites. Comparable levels of transmittance have been achieved for Er:Y_2O_3-MgO ceramics with varying levels of doping [18] (without specifying the thickness of the ceramic samples). This omission is significant because in materials prone to strong light scattering, even small increases in sample thickness can significantly reduce the transmittance. Given the absorption characteristics of Er^{3+} ions, it is plausible that the ceramics were much thinner than 1 mm. For potential laser applications, the thickness of the active element is crucial for reaching sufficiently high pump absorption. Efficient lasing at 2.8 μm has been achieved in 1.2 mm-thick sesquioxide ceramics doped with 7 at.% Er^{3+} [30]. In the case of Er:RE_2O_3-MgO composites, where the cubic sesquioxide phase comprises only half of the volume, it is reasonable to infer that the thickness of the ceramic elements should be at least comparable, if not greater, to target similar laser performances.

It can be speculated whether Er^{3+} ions are an interfering factor in achieving transparency of composites in the short wavelength spectral range. On the one hand, the presence of Er^{3+} ions contributes to a certain degree of lattice disorder due to the formation of a sesquioxide solid solution, $(Y_{1-x}Er_x)_2O_3$ or $(Gd_{1-x}Er_x)_2O_3$. This can enhance diffusion during sintering which is usually beneficial for pore healing. At the same time, diffusion of Mg^{2+} ions may also be enhanced, resulting in more pronounced grain growth. This increases Fresnel reflection losses at phase boundaries, potentially outweighing the benefits of reduced porosity. For example, when comparing the 1% Er:Sc_2O_3-MgO composite sintered at a temperature 100 °C lower than its counterpart, 1% Er:Lu_2O_3-MgO, it was found that the former material exhibited both a larger average grain size and reduced transmittance throughout the transparency window [14]. This difference is likely due to the greater solubility of MgO in Sc_2O_3 than in Lu_2O_3. Such observations highlight the complex interplay between dopant concentration and sintering conditions (in addition to the crucial steps of nanopowder synthesis and compaction) to achieve the desired optical properties attributed to fine grains, narrow grain size distribution, and uniform microstructure.

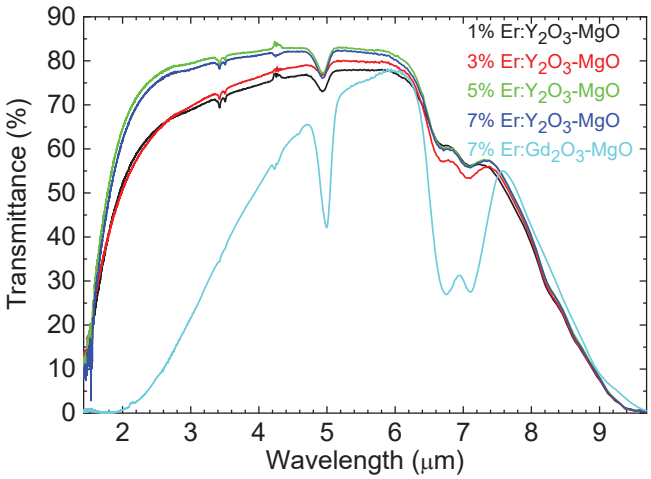

Figure 5. Infrared transmission spectra of Er:Y_2O_3-MgO and Er:Gd_2O_3-MgO composite ceramics.

The Raman spectra of the composites doped with 7 at.% Er^{3+} are reported in Fig. 6, each in direct comparison with that of its single-phase 7 at.% Er:RE_2O_3 ceramic counterpart, showing a maximum phonon energy of 573 cm^{-1} for Er:Gd_2O_3-MgO and 595 cm^{-1} in the case of Er:Y_2O_3-MgO. For the body-centered cubic (C-type) RE_2O_3 structure, the factor group

analysis predicts the irreducible representations for the optical (Γ_{op}) modes at the Γ-point ($\boldsymbol{k} = 0$) as follows: $\Gamma_{op} = 4A_g + 4E_g + 14F_g + 5A_{2u} + 5E_u + 16F_u$. Out of these, 22 modes (A_g, E_g and F_g) are Raman-active [31,32]. The measured Raman spectra clearly identify the presence of the cubic sesquioxide phase [33]. For the Er:Y_2O_3-MgO and Er:Gd_2O_3-MgO ceramics, a total of 12 and 16 modes are observed, respectively, and the most intense modes (at 378 cm^{-1} and 363 cm^{-1}, respectively) are assigned to $A_g + F_g$ vibrations. The low-phonon-energy behavior of the Er:Gd_2O_3-MgO composite is favorable for reducing the multiphonon non-radiative relaxation from Er^{3+} excited-states responsible for near- and mid-infrared luminescence [34].

Magnesium oxide has a weak Raman response with a strong effect of the crystal size on the intensity of lattice vibrations. Microcrystals of MgO, if Raman-active, are expected to give rise to two peaks, one at ~280 cm^{-1}, and another at ~446 cm^{-1} [35]. The comparison of the measured Raman spectra of the Er:RE_2O_3-MgO composites with those for single-phase ceramics of Gd_2O_3 and Y_2O_3, Fig. 6(a,b), reveals no appearance of any prominent additional peaks for the composite materials with respect to those of magnesia-free ceramics. This suggests that the Raman contributions of the MgO fraction are probably silent. However, the Raman spectra of the cubic sesquioxide phases within the composites are slightly different from those for the single-phase ceramics. For both Er:RE_2O_3-MgO composites, the Raman peaks are shifted to higher energies and broadened. For example, for Er:Y_2O_3-MgO, the dominant Raman mode appears at 378.1 cm^{-1} (bandwidth: 9.3 cm^{-1}) while for Er:Y_2O_3, it is found at 376.2 cm^{-1} and it is more narrow (bandwidth: 7.4 cm^{-1}). This can be explained by the suggested dissolution of Mg within the sesquioxide grains.

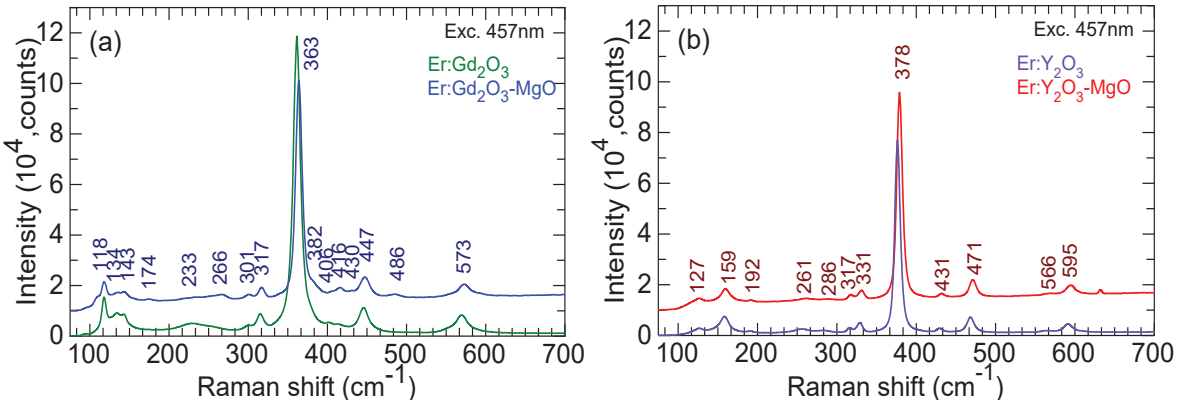

Figure 6. Raman spectra of 7 at.% Er:RE_2O_3-MgO composites, each compared with the respective single-phase 7 at.% Er:RE_2O_3 sesquioxide ceramics: (a) RE = Gd, and (b) RE = Y. *Numbers* indicate the Raman peak frequencies in cm^{-1}, λ_{exc} = 457 nm.

Owing to the high enough transparency of the Er:R_2O_3-MgO composite in the near-infrared spectral range, we were able to clearly resolve the absorption bands of Er^{3+} ions related to transitions from the ground state to both the $^4I_{13/2}$ and the $^4I_{11/2}$ excited manifolds. Figure 7 shows the absorption spectrum of Er^{3+} ions in Y_2O_3-MgO, expressed in absorption coefficient, α_{abs}. For the $^4I_{15/2} \rightarrow {}^4I_{11/2}$ transition, the maximum absorption coefficient amounts to 1.36 cm^{-1} at 971 nm and for the $^4I_{15/2} \rightarrow {}^4I_{13/2}$ one, the absorption is much stronger, expressed by α_{abs} = 8.45 cm^{-1} at 1536 nm.

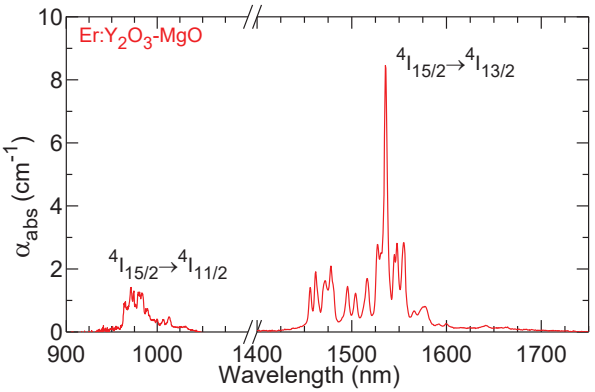

Figure 7. Er^{3+} absorption bands (the $^4I_{15/2} \rightarrow {}^4I_{11/2}$ and $^4I_{15/2} \rightarrow {}^4I_{13/2}$ transitions) in the 7 at.% Er:Y_2O_3-MgO composite.

The normalized luminescence spectra of Er^{3+} ions in both the Gd_2O_3-MgO and Y_2O_3-MgO composites are presented in Fig. 8. In the visible, Fig. 8(a), the two prominent emissions are in the green at ~550 nm, and in the red at ~670 nm. They are assigned respectively to the radiative transitions to the ground state from the thermally coupled $^2S_{3/2} + {}^2H_{11/2}$ multiplets and from the $^4F_{9/2}$ manifold. The spectra of visible luminescence of the two composites are rather similar but exhibit a blue-shift for gadolinia-base composite which is ascribed to the different crystal-field strengths for cubic yttria and gadolinia. The luminescence spectra in the near-IR, covering the ~0.98 µm emission from the $^4I_{11/2}$ manifold and the ~1.5 µm emission from the $^4I_{13/2}$ one, Fig. 8(b), show a similar behavior.

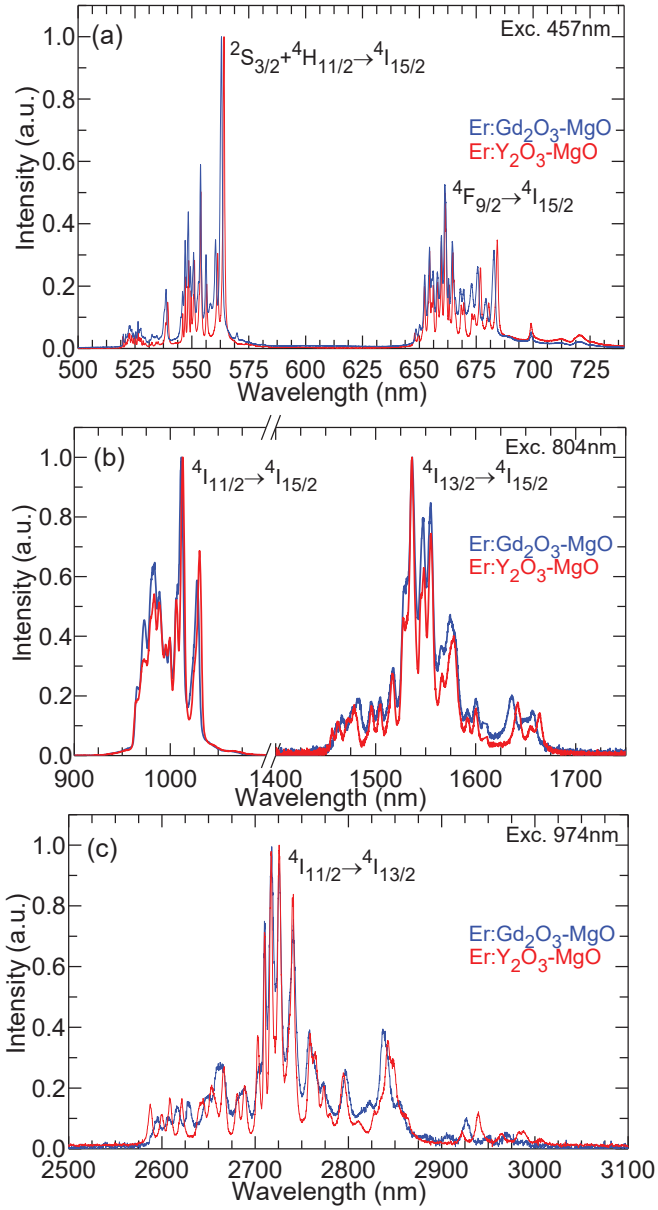

Figure 8. Luminescence spectra of Er^{3+} ions in 7 at.% Er:RE_2O_3-MgO composites: (a) visible emissions, λ_{exc} = 457 nm; (b) near-infrared emissions, λ_{exc} = 804 nm; (c) mid-infrared emission, λ_{exc} = 974 nm.

The spectra of mid-infrared luminescence, Fig. 8(c), are broad, spanning from 2.58 to 3.04 μm; this luminescence is assigned to the $^4I_{11/2} \longrightarrow {}^4I_{13/2}$ Er^{3+} transition[19]. The spectra contain several narrow intense peaks at 2710, 2717, 2726, and 2741 nm (for both composites), and a broad and less intense band at longer wavelengths, at 2837 nm (Er:Y_2O_3-MgO, bandwidth: 13 nm) or 2842 nm (Er:Gd_2O_3-MgO, bandwidth: 15 nm), which is the most usual set of wavelengths for achieving laser operation with Er^{3+}-doped cubic sesquioxides, given the reabsorption from the terminal laser level and the structured water vapor absorption in air within this spectral range.

Figure 9 shows the comparison between the mid-infrared emission spectra of erbium ions for the single-phase 7 at.% Er:Y_2O_3 ceramic and the 7 at.% Er:Y_2O_3-MgO composite. The spectral features of the two ceramics are visibly very similar, which suggests that the possible contribution of magnesia to the change in the local environment of active ions, if

any, is relatively weak. This, in turn, seems to confirm that all emitting erbium ions reside in the cubic sesquioxide phase.

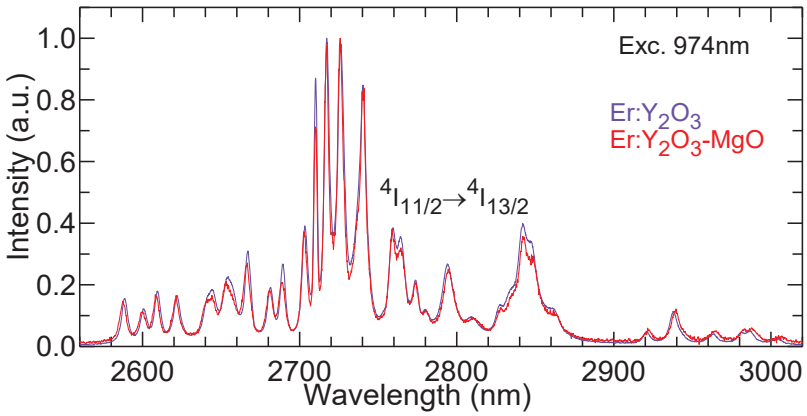

Figure 9. Comparison of mid-infrared luminescence spectra of Er^{3+} ions in the 7 at.% Er^{3+}-doped Y_2O_3 ceramic and its composite counterpart Y_2O_3-MgO, λ_{exc} = 974 nm.

The luminescence dynamics from the $^4I_{11/2}$ and $^4I_{13/2}$ Er^{3+} manifolds (the upper and lower laser levels for the mid-infrared laser transition) in the fabricated composites were studied under resonant excitation. The ceramic samples were finely powdered to reduce the effect of radiation trapping. The luminescence decay curves for 7 at.% Er^{3+}-doped RE_2O_3-MgO ceramics are reported in Fig. 10. One can immediately notice that, considering the same Er^{3+} doping level, while the mean luminescence lifetime of the $^4I_{11/2}$ level is consistently lower than that of the $^4I_{13/2}$ manifold, the two lifetimes are much closer in the case of Gd_2O_3-MgO. This is due to the weaker non-radiative path from the $^4I_{11/2}$ level in cubic gadolinia related to its lower-energy phonon spectrum. This makes Er:RE_2O_3-MgO composites appealing for laser emission in the mid-infrared.

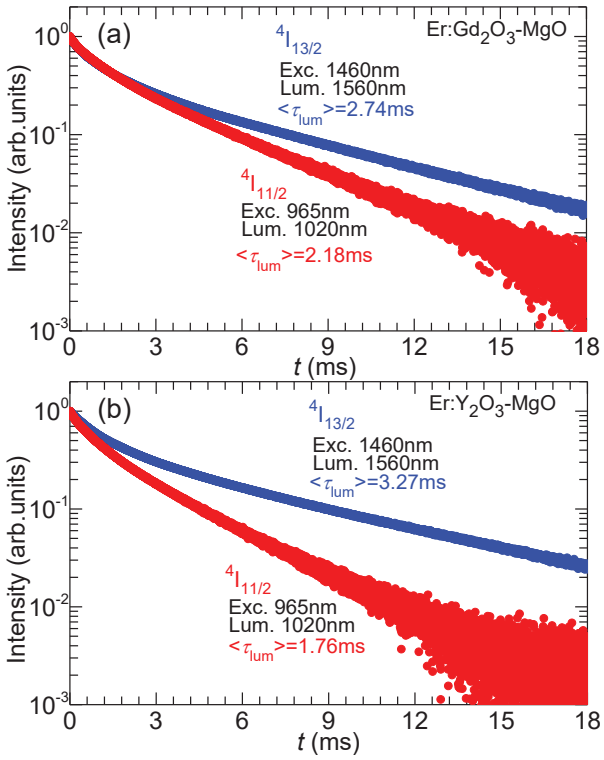

Figure 10. Luminescence decay curves for the $^4I_{13/2}$ and $^4I_{11/2}$ Er^{3+} states in the 7 at.% Er:RE_2O_3-MgO composites measured under resonant excitation, $<\tau_{lum}>$ - mean luminescence lifetime.

Table 3 reports the average luminescence lifetimes for all the studied composites, showing how the lifetime ratio between the $^4I_{11/2}$ and $^4I_{13/2}$ Er^{3+} manifolds in Er:Y_2O_3-MgO gradually increases with the erbium doping increasing from 1 at.% (lifetime ratio = 0.33) to 7 at.% (lifetime ratio = 0.54).

Table 3. Luminescence lifetimes of the $^4I_{13/2}$ and $^4I_{11/2}$ Er^{3+} states in the Er:RE_2O_3-MgO composites.

Composite	**Er^{3+} doping, at.%**	**Luminescence lifetime, ms**	
		$^4I_{13/2}$	**$^4I_{11/2}$**
Gd_2O_3-MgO	7	2.74	2.18
Y_2O_3-MgO	1	7.23	2.36
	3	6.02	2.34
	5	4.85	2.12
	7	3.27	1.76

5. Conclusions

This study has demonstrated the potential of Er:Y_2O_3-MgO and Er:Gd_2O_3-MgO nanocomposite ceramics as optical materials with appealing emission properties in the mid-infrared spectral range. The luminescence spectra of Er^{3+} ions in both composites show similarities in the visible, near-, and mid-IR emissions, with a notable blue-shift for the gadolinia-based ceramic. The broad spectrum of mid-IR luminescence spanning from ~2.6 to 3.0 μm is consistent with the $^4I_{11/2} \longrightarrow {}^4I_{13/2}$ Er^{3+} transition in the cubic sesquioxide phase. Mid-IR Er lasers operating on this transition are preferably pumped at 1.5 μm to the terminal laser manifold, $^4I_{13/2}$, employing an energy-transfer upconversion process, $^4I_{13/2} + {}^4I_{13/2} \rightarrow {}^4I_{15/2} + {}^4I_{9/2}$. The efficiency of this process increases with higher concentrations of Er^{3+} ions in the composite.

Raman peaks of the erbium-doped cubic sesquioxide phase in both composites are shifted to higher energies and broadened compared to single-phase Er:Y_2O_3 and Er:Gd_2O_3 ceramics. Together with XRD data and SEM/EDX elemental distribution maps, this may indicate some solubility of MgO in the sesquioxide phase of the composites. At the same time, the luminescence spectrum of Er^{3+} ions in the composites shows only minor changes compared to the spectra for single phase ceramics.

Acknowledgements

The study was funded by the Russian Science Foundation (Research Project No. 22-73-10084), French Agence Nationale de la Recherche (ANR) (project SPLENDID2, ANR-19-CE08-0028), “RELANCE” Chair of Excellence project funded by the Normandy Region, Région Normandie, France (Contrat de plan État-Région (CPER)).

References

[1] Z. Liu, A. Ikesue, J. Li, Research progress and prospects of rare-earth doped sesquioxide laser ceramics, J. Eur. Ceram. Soc. 41 (2021) 3895–3910. https://doi.org/10.1016/j.jeurceramsoc.2021.02.026.

[2] O. V. Palashov, A. V. Starobor, E.A. Perevezentsev, I.L. Snetkov, E.A. Mironov, A.I. Yakovlev, S.S. Balabanov, D.A. Permin, A. V. Belyaev, Thermo-Optical Studies of Laser Ceramics, Materials (Basel). 14 (2021) 3944. https://doi.org/10.3390/ma14143944.

[3] Y. Sato, M. Arzakantsyan, J. Akiyama, T. Taira, Anisotropic Yb:FAP laser ceramics by micro-domain control, Opt. Mater. Express. 4 (2014) 2006. https://doi.org/10.1364/OME.4.002006.

[4] A. Krell, G.M. Baur, C. Dahne, Transparent sintered sub-µm Al2O3 with infrared transmissivity equal to sapphire, in: R.W. Tustison (Ed.), 2003: p. 199. https://doi.org/10.1117/12.485770.

[5] J. Klimke, M. Trunec, A. Krell, Transparent Tetragonal Yttria-Stabilized Zirconia Ceramics: Influence of Scattering Caused by Birefringence, J. Am. Ceram. Soc. 94 (2011) 1850–1858. https://doi.org/10.1111/j.1551-2916.2010.04322.x.

[6] H. Furuse, T. Okabe, H. Shirato, D. Kato, N. Horiuchi, K. Morita, B.-N. Kim, High-optical-quality non-cubic Yb3+ -doped Ca10(PO4)6F2 (Yb:FAP) laser ceramics, Opt. Mater. Express. 11 (2021) 1756. https://doi.org/10.1364/OME.426701.

[7] Y. Zhang, B. Mei, W. Li, Y. Yang, G. Yi, Z. Zhou, Z. Liu, Fabrication and spectral properties of Nd:S-FAP transparent ceramics by simple route of HP method, J. Alloys Compd. 820 (2020) 153171. https://doi.org/10.1016/j.jallcom.2019.153171.

[8] D. Permin, M. Nazmutdinov, S. Kurashkin, S. Balabanov, A. Belyaev, A. Novikova, V. Koshkin, Fabrication and Luminescent Properties of Er-Doped Sr5(PO4)3F Ceramics, Inorganics. 11 (2023) 57. https://doi.org/10.3390/inorganics11020057.

[9] M.D. Nazmutdinov, D.A. Permin, S.S. Balabanov, S.A. Melnikov, K.E. Smetanina, T.S. Pozdova, Fabrication and study of the strontium fluoroarsenate Sr5(AsO4)3F (SFAs) transparent ceramics, Open Ceram. 17 (2024) 100543. https://doi.org/10.1016/j.oceram.2024.100543.

[10] J. Akiyama, Y. Sato, T. Taira, Laser Demonstration of Diode-Pumped Nd3+ -Doped Fluorapatite Anisotropic Ceramics, Appl. Phys. Express. 4 (2011) 022703. https://doi.org/10.1143/APEX.4.022703.

[11] D.C. Harris, L.R. Cambrea, L.F. Johnson, R.T. Seaver, M. Baronowski, R. Gentilman, C. Scott Nordahl, T. Gattuso, S. Silberstein, P. Rogan, T. Hartnett, B. Zelinski, W. Sunne, E. Fest, W. Howard Poisl, C.B. Willingham, G. Turri, C. Warren, M. Bass, D.E. Zelmon, S.M. Goodrich, Properties of an Infrared-Transparent MgO:Y2O3 Nanocomposite, J. Am. Ceram. Soc. 96 (2013) 3828–3835. https://doi.org/10.1111/jace.12589.

[12] N. Wu, X. Li, J.-G. Li, Q. Zhu, X. Sun, Fabrication of Gd2O3-MgO nanocomposite optical ceramics with varied crystallographic modifications of Gd2O3 constituent, J. Am. Ceram. Soc. 101 (2018) 4887–4891. https://doi.org/10.1111/jace.15884.

[13] D.A. Permin, V.A. Koshkin, S.S. Balabanov, A.V. Belyaev, O.V. Timofeev, I.L. Snetkov, P.A. Popov, Dy2O3–MgO composite ceramics: Fabrication and properties, Ceram. Int. (2023). https://doi.org/10.1016/j.ceramint.2023.12.410.

[14] D. Permin, A. Belyaev, V. Koshkin, S. Kurashkin, S. Balabanov, K. Smetanina, M. Boldin, O. Klyusik, Erbium-Doped Lu2O3-MgO and Sc2O3-MgO IR-Transparent Composite Ceramics, Nanomaterials. 13 (2023). https://doi.org/10.3390/nano13101620.

[15] N.A. Safronova, R.P. Yavetskiy, O.S. Kryzhanovska, M.V. Dobrotvorska, A.E. Balabanov, I.O. Vorona, A.V. Tolmachev, V.N. Baumer, I. Matolínová, D.Y. Kosyanov, O.O. Shichalin, E.K. Papynov, S. Hau, C. Gheorghe, A novel IR-transparent Ho3+:Y2O3–MgO nanocomposite ceramics for potential laser applications, Ceram. Int. 47 (2021) 1399–1406. https://doi.org/10.1016/j.ceramint.2020.08.263.

[16] Y. Wang, H. Mu, N. Wu, M. Zhang, Q. Zhu, X. Sun, X. Li, Effects of Ho3+ concentration on the fabrication and properties of Ho: Y2O3-MgO nanocomposite for Mid-infrared laser

applications, Ceram. Int. 49 (2023) 10625–10633. https://doi.org/10.1016/j.ceramint.2022.11.250.
[17] V.L. Blair, Z.D. Fleischman, L.D. Merkle, N. Ku, C.A. Moorehead, Co-precipitation of rare-earth-doped Y2O3 and MgO nanocomposites for mid-infrared solid-state lasers, Appl. Opt. 56 (2017) B154. https://doi.org/10.1364/AO.56.00B154.
[18] H.J. Ma, W.K. Jung, Y. Park, D.K. Kim, A novel approach of an infrared transparent Er:Y2O3–MgO nanocomposite for eye-safe laser ceramics, J. Mater. Chem. C. 6 (2018) 11096–11103. https://doi.org/10.1039/C7TC05991D.
[19] A. Uvarova, P. Loiko, S. Kalusniak, E. Dunina, L. Fomicheva, A. Kornienko, S. Balabanov, A. Braud, P. Camy, C. Kränkel, Stimulated-emission cross-sections of trivalent erbium ions in the cubic sesquioxides Y2O3 , Lu2O3 , and Sc2O3, Opt. Mater. Express. 13 (2023) 1385. https://doi.org/10.1364/OME.487909.
[20] S. Balabanov, T. Evstropov, D. Permin, O. Postnikova, A. Praded, P. Popov, Thermal Conductivity of Yttria-Gadolinia Solid Solution Optical Ceramics in the Temperature Range 50–300 K, Inorganics. 10 (2022) 78. https://doi.org/10.3390/inorganics10060078.
[21] D.A. Permin, A. V. Belyaev, V.A. Koshkin, S.S. Balabanov, P.A. Popov, M.S. Boldin, A.A. Murashov, K.E. Smetanina, I. V. Ladenkov, Comparison of the Properties of the MgO–Y2O3 and MgO–Gd2O3 Ceramic Composites Obtained by the Method of Hot Compaction, J. Eng. Phys. Thermophys. 95 (2022) 1595–1603. https://doi.org/10.1007/s10891-022-02628-2.
[22] D.A. Permin, M.S. Boldin, A.V. Belyaev, S.S. Balabanov, A.V. Novikova, V.A. Koshkin, A.A. Murashov, I.V. Ladenkov, A.A. Popov, E.A. Lantsev, N.M. Khamaletdinova, IR-transparent MgO-Y2O3 ceramics by self-propagating high-temperature synthesis and spark plasma sintering, Ceram. Int. 46 (2020) 15786–15792. https://doi.org/10.1016/j.ceramint.2020.03.124.
[23] D.A. Permin, M.S. Boldin, A.V. Belyaev, S.S. Balabanov, V.A. Koshkin, A.A. Murashov, I.V. Ladenkov, E.A. Lantsev, K.E. Smetanina, N.M. Khamaletdinova, IR-transparent MgO-Gd2O3 composite ceramics produced by self-propagating high-temperature synthesis and spark plasma sintering, J. Adv. Ceram. (2021). https://doi.org/10.1007/s40145-020-0434-1.
[24] D.A. Permin, A. V. Belyaev, S.S. Balabanov, V.A. Koshkin, M.S. Boldin, A. V. Novikova, O. V. Timofeev, Z.K. Gashpar, I. V. Ladenkov, Effect of Composition on the Structure and Properties of MgO/Y2O3 Composite Ceramics, Inorg. Mater. 58 (2022) 643–650. https://doi.org/10.1134/S0020168522060085.
[25] A. V. Tresvyatskii, S. G., Lopato, L. M., Ogorodnikova, A. A., Shevchenko, Phase diagrams of the systems formed by yttrium, erbium, and ytterbium oxides with magnesium oxide, Inorg. Mater. (USSR) (Engl. Transl.). 7 (1971) 1798–1801.
[26] L.M. Lopato, A.A. Ogorodnikova, A.V. Shevchenko, Phase diagrams of the systems of samarium, gadolinium and dysprosium oxides with magnesium oxide, Dopov. Akad. Nauk Ukr. RSR, Ser. B Geol., Khim. Biol. Nauk. 32 (1970) 1106–1108.
[27] D.A. Permin, A. V. Belyaev, V.A. Koshkin, S.S. Balabanov, M.S. Boldin, I. V. Ladenkov, I.G. Fedotova, Effect of Hot Pressing Conditions on the Microstructure and Optical Properties of MgO–Y2O3 Composite Ceramics, Inorg. Mater. 57 (2021) 858–866. https://doi.org/10.1134/S0020168521080082.
[28] L. Liu, K. Morita, T.S. Suzuki, B.-N. Kim, Effect of volume ratio on optical and mechanical properties of Y2O3-MgO composites fabricated by spark-plasma-sintering process, J. Eur. Ceram. Soc. 41 (2021) 2096–2105. https://doi.org/10.1016/j.jeurceramsoc.2020.10.074.
[29] N. Wu, X. Li, M. Zhang, Y. Ren, Q. Zhu, H. Peng, H. Ru, X. Sun, Synthesis of nanopowders with low agglomeration by elaborating Φ values for producing Gd2O3-MgO nanocomposites with extremely fine grain sizes and high mid-infrared transparency, J. Eur. Ceram. Soc. 41 (2021) 2898–2907. https://doi.org/10.1016/j.jeurceramsoc.2020.11.019.
[30] S. Balabanov, P. Loiko, L. Basyrova, D. Permin, D. Kosyanov, T. Evstropov, S. Filofeev, A. Braud, P. Camy, Mid-infrared laser operation of (Er0.07La0.10Y0.83)2O3 sesquioxide ceramic, Laser

Phys. Lett. 20 (2023) 045801. https://doi.org/10.1088/1612-202X/acbce4.
[31] M. V. Abrashev, N.D. Todorov, J. Geshev, Raman spectra of R2O3 (R — rare earth) sesquioxides with C-type bixbyite crystal structure: A comparative study, J. Appl. Phys. 116 (2014). https://doi.org/10.1063/1.4894775.
[32] N.D. Todorov, M. V. Abrashev, V. Marinova, M. Kadiyski, L. Dimowa, E. Faulques, Raman spectroscopy and lattice dynamical calculations of Sc2O3 single crystals, Phys. Rev. B. 87 (2013) 104301. https://doi.org/10.1103/PhysRevB.87.104301.
[33] K. Eremeev, P. Loiko, S. Balabanov, T. Evstropov, D. Permin, O. Postnikova, V. Petrov, P. Camy, A. Braud, Spectroscopy of thulium ions in solid-solution sesquioxide laser ceramics: Inhomogeneous spectral line broadening, crystal-field engineering and C3i sites, Opt. Mater. (Amst). 148 (2024) 114791. https://doi.org/10.1016/j.optmat.2023.114791.
[34] S. Normani, P. Loiko, L. Basyrova, A. Benayad, A. Braud, E. Dunina, L. Fomicheva, A. Kornienko, A. Hideur, P. Camy, Mid-infrared emission properties of erbium-doped fluorite-type crystals, Opt. Mater. Express. 13 (2023) 1836. https://doi.org/10.1364/OME.482402.
[35] K. Ishikawa, N. Fujima, H. Komura, First-order Raman scattering in MgO microcrystals, J. Appl. Phys. 57 (1985) 973–975. https://doi.org/10.1063/1.334701.